



Automatic discrimination of actinic keratoses from clinical photographs



Panagiota Spyridonos^{a,*}, Georgios Gaitanis^b, Aristidis Likas^c, Ioannis D. Bassukas^b

^a Department of Medical Physics, Faculty of Medicine, School of Health Sciences, University of Ioannina, University Campus, 45110 Ioannina, Greece

^b Department of Skin and Venereal Diseases, Faculty of Medicine, School of Health Sciences, University of Ioannina, University Campus, 45110 Ioannina, Greece

^c Department of Computer Science & Engineering, University of Ioannina, University Campus, 45110 Ioannina, Greece

ARTICLE INFO

Keywords:

Actinic keratosis
Clinical photography
Color texture analysis
Local binary patterns
Textons
Support vector machines

ABSTRACT

Background and Objective: Actinic keratoses (AK) are common premalignant skin lesions that can progress to invasive skin squamous cell carcinoma (sSCC). The subtle accumulation of multiple AK in aging individuals increases the risk of sSCC development, and this underscores the need for efficient treatment and patient follow-up. Our objectives were to develop a method based on color texture analysis of standard clinical photographs for the discrimination of AK from healthy skin and subsequently to test the developed approach in the quantification of field-directed treatment interventions.

Methods: AK and healthy skin in clinical photographs of 22 patients were demarcated by experts and regions of interest (ROIs) of 50×50 pixels were cropped. The data set comprised 6010 and 13915 ROIs from AK and healthy skin, respectively. Color texture features were extracted using local binary patterns (LBP) or texton frequency histograms and evaluated employing a support vector machine (SVM) classifier. Classifier evaluation was performed using a leave-one-patient-out scheme in RGB, YIQ and CIE-Lab color spaces. The best configuration of the SVM model was tested using 157 AK and 216 healthy skin rectangular regions of arbitrary size. AK treatment outcome was evaluated in an additional group of eight patients with 32 skin lesions.

Results: The best configuration of the discrimination model was achieved by employing LBP color texture descriptors estimated from the Y and I components of the YIQ color space. The sensitivity and specificity of the SVM model were 80.1% and 81.1% at ROI level and 89.8% and 91.7% at region level, respectively. Based on the classifier results the quantitative AK reduction was 83.6%.

Conclusions: It is important that patients with AK seek evaluation for treatment to reduce the risk of disease progression. Efficient patient follow-up and treatment evaluation require cost-effective and easy to use approaches. The proposed SVM discrimination model based on LBP color texture analysis renders clinical photography a practical, widely available and cost-effective tool for the evaluation of AK burden and treatment efficacy.

1. Introduction

Actinic keratoses (AK) are common premalignant lesions of the skin, mostly affecting individuals of European ancestry [1] and constitute a significant workload in dermatology outpatient clinics worldwide [2]. AK result from chronic exposure to ambient ultraviolet radiation, thus they are mostly located on the chronically sun-exposed skin of older adults. With increasing age susceptible individuals develop multiple clinical and subclinical AK lesions that coexist in carcinogen-exposed skin areas (“field cancerization”) [3]. The biological behavior of an individual AK may vary: it can remain relatively stable in form and size for a long period or spontaneously involute and ultimately disappear. On the other hand, some lesions may evolve into a hyperplastic, hyperkeratotic state and ultimately a minority of them (<0.1% of lesions/per year) may

progress to skin squamous cell carcinoma (sSCC), a potentially lethal tumor [4,5]. However, since 60%–80% of sSCCs arise in AK fields, timely treatment of these lesions is anticipated to prevent progression [6–8].

In practice, and during the examination of a skin field, it is common for the clinician to document the presence of multiple, unevenly distributed, partly coalescent AK of different sizes. In these cases, evaluating disease burden at baseline and quantifying treatment efficacy is a challenging, real-life problem. The latter is highlighted in corresponding clinical studies where the use of subjective means to measure AK burden results in suboptimal interobserver agreement [9–11].

Research on computer vision systems for the evaluation of skin diseases is a continuously growing subfield of medical image analysis [12–14]. High-quality clinical images and specialized instruments that magnify deeper skin tissues have been coupled with automated detection

* Corresponding author.

E-mail addresses: pspyrid@cc.uoi.gr (P. Spyridonos), ggaitan@cc.uoi.gr (G. Gaitanis), arly@cs.uoi.gr (A. Likas), ibassuka@cc.uoi.gr (I.D. Bassukas).

systems to offer valuable computer-aided diagnostic tools for the assessment of keratinocytic skin malignancies. To date, non-invasive imaging of AK has addressed the identification and differential diagnosis of isolated skin lesions, employing techniques such as the cost-effective digital dermoscopy or the more sophisticated reflectance confocal microscopy (RCM) and high-definition optical coherence tomography (OCT). The diagnostic accuracy of OCT images has been assessed using ensemble classifiers and support vector machine (SVM) models in the differentiation of AK from basal cell carcinomas (BCC) [15]. Recently, the *in vivo* optical properties of facial AK subtypes and sSCC were quantified by high-definition OCT and a decision tree diagnostic algorithm for the discrimination of sun-damaged facial skin from AK subtypes and SCC was proposed [16]. Likewise, classification trees with morphologic RCM characteristics have been used for the discrimination of AK from normal skin [17] and to combine dermoscopic signs that predict the relevant histopathological findings in AK diagnosis [18]. Also, a Bayesian classifier and 3D features obtained by a sophisticated stereo image system have been used to automatically distinguish between keratinocytic malignancies [19]. In addition, rather cumbersome, non-portable equipment employing cross-polarized light and fluorescence has been proposed for skin cancer screening purposes, including the diagnosis of AK [20].

Conventional skin biopsy and histopathological examination remain the gold standard for confirming the diagnosis of AK. In general, most of the aforementioned non-invasive imaging approaches intend to substitute biopsy for the diagnosis of selected skin lesions [21]. However, regarding AK, the fundamental limitation of all aforementioned methods is that they are spatially elective, capable of supporting the recognition of few selected lesions per-patient and thus unsuitable for “field” quantification purposes. For example employing dermoscopy a relative small skin area can be evaluated per field of view (corresponding to approximately 4 cm² for a common commercially available digital dermatoscope; DermLite, PhotoSystem, 3Gen, LLC, Dana Point, CA, U.S.A.). Clinical photography on the other hand can provide morphological information of whole anatomic skin regions that in addition can harbor multiple AK, e.g. the skin of the face or the balding scalp, a quasi ‘scanning modality’ for morphological alterations of the skin surface.

The applicability of standard clinical photographs in the evaluation of keratinocytic premalignancies has been addressed in a limited number of studies. Using clinical photographs a hierarchical classification system based on the k-nearest neighbors (K-NN) model for discrimination between benign and malignant skin growths has been proposed [22]. Furthermore, automatic delineation of AK areas on clinical photographs has been elaborated using color space transforms and morphological features for erythema detection [23].

In this study, we developed an SVM model for discrimination of AK from normal skin, based on color texture analysis of non-standardized clinical photographs. Our aim was to use photography to quantify AK burden and to evaluate the outcome of treatment interventions that target skin cancerization fields. To the best of our knowledge, the present study is the first image analysis approach towards the quantification of AK burden for efficient treatment evaluation and patient follow-up by means of clinical photography.

2. Materials and methods

2.1. Acquisition of clinical photographs

Institutional approval was granted and patients with at least one biopsy-proven AK were recruited from a dermatology outpatients clinic; all patients gave informed consent for the photographic assessment of their skin lesions. A total of 30 patients (24 men) were included (mean age: 78 [range: 68–85] years). Photographs from 22 patients were used for the model development and the rest for evaluating AK burden reduction after treatment. Photographs were acquired using a Nikon D610 camera with a spatial resolution of 6016 × 4016 pixels. A 60 mm

prime lens was adapted with two adjustable crossed polarized filters to minimize unwanted glare and a SIGMA EM-140 Macro ring flash. Images were rescaled to an equal final size of 50 pixels per millimeter employing as internal standards stickers attached to the skin (MACO Round Color Coding Labels, 0.635 cm [1/4 inch] in diameter, USA).

The same physician took all images at baseline and during follow-up visits with the volunteers seated. A detailed description of image acquisition is given in Fig. 1.

2.2. Discrimination model implementation

The automatic discrimination of facial AK lesions from healthy skin was addressed as a two-class classification problem, using the SVM classifier.

SVM is an advanced and extensively used classification method that has been successfully applied to a variety of real-world data analysis problems (text categorization, image recognition, bioinformatics and medical decision), mostly providing improved results compared with other techniques [24–26]. SVM is currently considered the standard method used to build a classifier from training data, especially in problems with continuous input features, as in our case. Further details on the SVM classifier can be found in Ref. [27].

In this study, the radial basis function (RBF) kernel was used for the SVM implementation. The SVM classifier performance depends on the choice of the parameter (C) which is also known as box constraint and the scaling factor (γ) which is the inverse width of the RBF kernel. We tested various pairs of (C, γ) values and we selected the one with the best predictive accuracy for both classes.

To train and validate the SVM classifier, AK and healthy skin 50 × 50 pixel regions of interest (ROIs) were cropped from areas demarcated by experts in each photograph (Fig. 2). A 50 × 50 pixel ROI is about one mm² and is the largest ROI adequate to sample the smallest demarcated by experts skin area. The data set comprised 6010 and 13915 ROIs of AK and healthy skin, respectively, extracted from 22 patients (Table 1).

Two different SVM models were constructed and evaluated. In the first model, each ROI is represented by its color local binary pattern (LBP) histogram (SVM_{LBP} model). In the second model, each ROI is represented by its texton frequency histogram (SVM_{Textons} model).

Both SVM models were evaluated in terms of their sensitivity and specificity. For this, the number of true positives (TP), false negatives (FN), true negatives (TN) and false positives (FP) was obtained by each model. TN is the number of healthy skin ROIs correctly identified, FN is the number of AK ROIs incorrectly identified as healthy skin, TP is the number of AK ROIs correctly identified and FP is the number of healthy skin ROIs incorrectly identified as AK. Sensitivity is the probability that the SVM model will respond positively when tested on the AK ROI:

$$\text{Sensitivity} = \frac{TP}{(TP + FN)} \quad (1)$$

Specificity is the probability that the SVM model will respond negatively when tested on the healthy skin ROI:

$$\text{Specificity} = \frac{TN}{(TN + FP)} \quad (2)$$

Finally, the accuracy is defined as the probability that the SVM model will correctly classify both classes:

$$\text{Accuracy} = \frac{TP + TN}{TP + FP + TN + FN} \quad (3)$$

Evaluation of the discrimination models was performed using the leave-one-patient-out scheme, meaning that ROIs from all patients but one were used for the training and ROIs from the patient excluded for testing the model. To avoid overtraining the model in favor of the majority class (the healthy skin class), equal numbers of healthy skin and AK patterns were randomly selected from each patient in the training set.

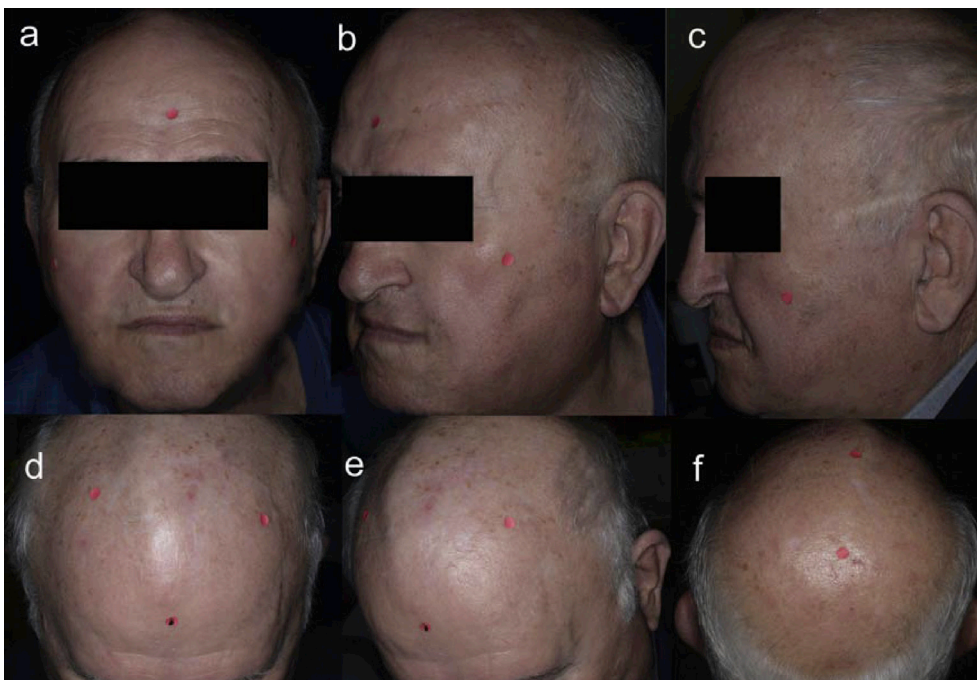


Fig. 1. For facial pictures, portrait images with the camera axis perpendicular to the photographed region at 0° (a), 45°/–45° (b) and 90°/–90° (c) angles to the coronal (sagittal) plane were acquired. The distance was adjusted to include the whole face from the chin to the top of the hair/scalp. For balding scalps three sets of landscape pictures were taken: one with the lower frame on the eyebrows and with an angle that positioned the ears in the middle of the frame (d). With this approach images from the forehead and the anterior half of the vertex scalp were suitable for analysis. Two additional images from both sides of the scalp were taken to include the ipsilateral vertex and forehead. For these images, the landscape frame was positioned on the eyebrows (lower frame) and the ipsilateral ear (the lateral frame) (e). Likewise, the nuchal area and the top of the scalp were photographed from the back, both perpendicularly to the nuchal area and at an angle that would position the lower frame on the hairline and the ears in the middle of the frame (f).

The best configuration of the SVM model was also tested at skin region level. That is, from each patient, up to 10 arbitrarily sized (box) regions of AK and healthy skin were selected. In total, 157 AK and 216 healthy skin regions were tested. A sliding window of 50 × 50 pixels is moved across the image region by 10 pixels overlapping in each translocation. In each sliding position, the 50 × 50 window is assigned by the SVM model as belonging to the AK class or the healthy skin class. The SVM model has been previously trained by regions from all patients except the patient under testing. The skin region under testing was finally recognized as AK or healthy skin according to the majority class assigned to the 50 × 50 windows of that region.

To visualize the results, SVM outputs were converted to posterior probabilities in the range [0 1] [28]. In each sliding position a pseudo-color was assigned using a color map that corresponds a probability value of 0 to blue (healthy class) and a probability value of 1 to yellow (AK

class). Explanatory examples are given in Fig. 3.

SVM models were implemented using Matlab (R2015b, The Math-Works) and run on a personal computer with a 64-bit operating system, 2.4 GHz CPU and 12 GB memory.

2.3. Color texture analysis

The clinical diagnosis of AK relies on the recognition of certain macromorphological characteristics. A typical AK appears as a white, scaly lesion of variable thickness with surrounding redness [1,3]. Upon palpation AK are detected due to their distinctive sandpaper-like texture, supporting our strategy of using color texture analysis for the discrimination of facial AK from normal skin.

Two main approaches to feature extraction for color texture analysis are often used and consist of:

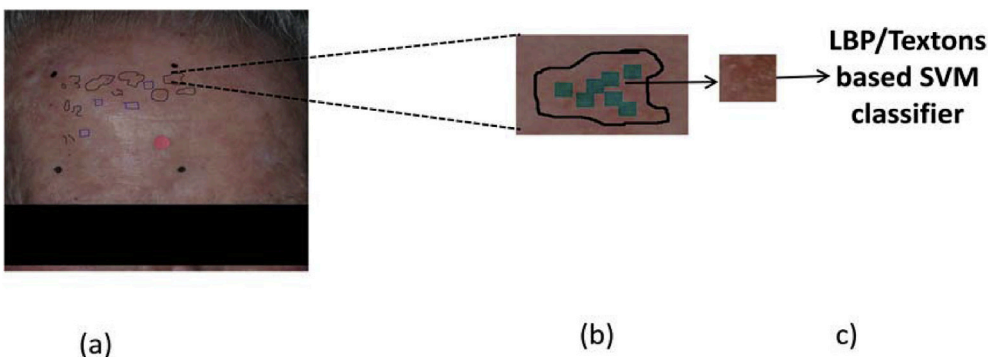


Fig. 2. ROI selection for model implementation starting from areas demarcated by experts in a clinical photograph. (a) Patient photograph with regions demarcated by experts: AK lesions delimited by black and healthy regions delimited by blue borders. A round color coding label (red) was used as the internal standard – all images were rescaled to an equal final size of 50 pixels per mm. (b) From demarcated skin areas standardized 50 × 50 pixel ROIs were extracted and (c) from each ROI color LBP and texton features were extracted to feed the SVM classifier. The greater rectangular field delimited by the four black dots corresponds to a 25 cm² treatment area. (For interpretation of the references to colour in this figure legend, the reader is referred to the web version of this article.)

Table 1
Number of AK and healthy ROIs (50 × 50 pixels) extracted from each patient.

Patient	AK ROIs	Normal skin ROIs
1	147	216
2	425	1275
3	87	340
4	230	880
5	250	375
6	546	1835
7	225	60
8	537	193
9	66	193
10	536	332
11	197	47
12	698	1217
13	459	1660
14	87	563
15	12	18
16	330	658
17	194	1359
18	72	108
19	586	1595
20	168	683
21	66	48
22	92	260
Total	6010	13915

- i. Applying gray-level texture analysis techniques to each color channel separately
- ii. Extracting textural information from the luminance plane along with pure chrominance features.

Both methods have resulted in substantial improvement in the performance of standard gray-level texture analysis techniques [29].

In the present study, we adopted the first method of extending the gray-level texture to channel-wise color texture analysis. More specifically, we considered channel-wise color LBP and raw pixel representation textons. Both LBP and texton-based approaches have exhibited excellent texture classification performance on standard texture databases [30,31].

RGB color space is the standard format for displaying color digital images. A problem with this color representation is that it is device-dependent. Moreover, RGB values are very sensitive to illumination intensity and color changes because of the high correlation among the R, G and B components. Thus, although RGB is suitable for color display, it is not preferred for color analysis. RGB space can achieve satisfactory color discrimination accuracy under controlled illumination, however, this is not retained under variable illumination conditions. Additionally, AK appear with variable colors. Thus absolute color evaluation is not useful in image analysis. For improved color processing RGB is commonly transformed to alternative spaces [29,32–34]. In this paper, along with RGB, YIQ and CIE-Lab color spaces were also investigated.

In the YIQ color model, the Y component is a measure of color luminance. The I component represents the hue and the Q component represents the saturation of the image. The YIQ space can partly reduce the correlation of the red, green and blue components in an image.

In the CIE-Lab color space, the L defines the lightness or the intensity of a color whereas **a** and **b** are the chromaticity components. Lab space can also control color and intensity information more independently.

YIQ has been proved to be an effective color space transformation for facial image analysis applications whereas CIE-Lab color space associates well with human vision systems [33].

2.4. Review of LBP features

Assuming a local circular region of a radius R consisting of P neighbors, the LBP operator is estimated by taking the difference of the center pixel with respect to its neighbors:

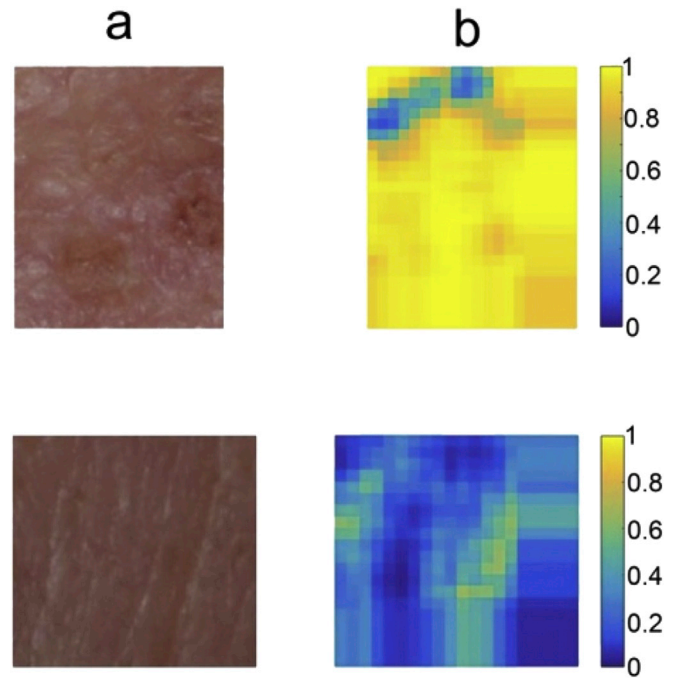


Fig. 3. Examples of application of the discrimination model to visualize and quantify AK burden in selected skin regions. **Top:** (a) A tested AK skin region of 250 × 200 pixels (left side) was separated into 336 50 × 50 pixel windows (10 pixel overlap of adjacent windows). (b) In each window SVM posterior probability was color-mapped to better visualize the automatic skin recognition results. The majority of the windows were positives (309/336; 92%) and the whole skin region was recognized as an AK lesion. **Bottom:** (a) A tested healthy skin region of 200 × 200 pixels was separated into 256 50 × 50 pixel windows (10 pixel overlap). (b) Color-mapped SVM posterior probabilities. The majority of the windows were negatives (231/256; 90.2%) and the whole skin region was recognized as healthy. (For interpretation of the references to colour in this figure legend, the reader is referred to the web version of this article.)

$$LBP_{P,R} = \sum_{p=0}^{P-1} s(g_p - g_c) 2^p \quad (4)$$

$$s(g_p - g_c) = \begin{cases} 1 & g_p \geq g_c \\ 0 & g_p < g_c \end{cases} \quad (5)$$

where g_c and g_p denote the values of the central pixel and its neighbor, respectively, and p is the index of the neighbor. The values of neighbors that are not in the center of grids are estimated by interpolation.

The U value of an LBP pattern is defined as the number of spatial transitions (bitwise 0/1 changes):

$$U(LBP_{P,R}) = |s(g_{P-1} - g_c) - s(g_0 - g_c)| + \sum_{p=1}^{P-1} |s(g_p - g_c) - s(g_{p-1} - g_c)| \quad (6)$$

It has been shown that only “uniform” patterns ($U \leq 2$) are essential patterns of local image texture [35]. For example, bit strings 00000000 (0 transitions) and 01111000 (two transitions) are uniform while 10001001 (four transitions) and 01010110 (six transitions) are not. Non-uniform patterns ($U > 2$) are grouped under the “miscellaneous” label. The mapping from $LBP_{P,R}$ to $LBP_{P,R}^{u2}$ reduces the different output values from 2^P to $P \times (P - 1) + 3$ (superscript u2 means that the uniform patterns have $U \leq 2$).

Further, to extract rotation-invariant LBP descriptors, the locally rotation-invariant pattern was adopted. This is defined as follows [36]:

$$LBP_{P,R}^{riu2} = \begin{cases} \sum_{p=0}^{P-1} s(g_p - g_c) & \text{if } U(LBP_{P,R}) \leq 2 \\ P + 1 & \text{otherwise} \end{cases} \quad (7)$$

The mapping from $LBP_{P,R}$ to $LBP_{P,R}^{riu2}$ results in $P + 2$ different output values.

After estimating the $LBP_{P,R}^{riu2}$ pattern in each pixel (i, j) , the texture of an ROI of 50×50 pixels is represented by building a histogram:

$$H(k) = \sum_{i=1}^{50} \sum_{j=1}^{50} f(LBP_{P,R}^{riu2}(i, j), k), \quad k \in [0, K] \quad (8)$$

$$f(x, y) = \begin{cases} 1, & x = y \\ 0, & \text{otherwise} \end{cases} \quad (9)$$

The aforementioned LBP operations (Eqs. (7)–(9)) are applied to each component of the YIQ (or CIE-Lab) color space. The final color LBP histogram of each ROI is obtained by concatenating the d individual channel LBP histograms into a single column vector with $d \times (P + 2)$ elements, where d is the number of color channels used from the YIQ (or CIE-Lab) color space.

2.5. Review of textons using image patch exemplars

There are two main approaches proposed in the literature for texton-based texture description, filter banks [37] or raw pixel representation [31]. Raw pixel representation has recently gained ground, exhibiting similar or even superior classification results compared with multi-scale, multi-orientation filter banks [31,38].

Irrespective of the approach used to describe texture information, implementing textons consists of the following processing steps: initially, a codebook (dictionary) of textons is created using a clustering algorithm such as k-means. To construct the texton codebook using the raw pixel representation approach, small-sized $N \times N$ (3×3 in the present case) local patches are extracted from each ROI in the training set and the raw pixel intensities of these square neighborhoods are column-reordered to form a $d \times N^2$ dimensional vector where d is the number of color channels used from the YIQ (or CIE-Lab) color space. All the patches from the training ROIs are aggregated and clustered. The set of cluster centers comprises the texton dictionary. Next, a texton histogram is computed for each ROI in the training set. For this, small patches (3×3) are extracted by sliding a window over each training ROI. Then, a histogram of textons is computed by comparing every patch representation in that ROI with

all textons in the dictionary using the Euclidean distance. A schematic overview of the herein applied texton feature extraction and classification procedures is given in Fig. 4.

2.6. Treatment evaluation of AK

Photographs at baseline and during follow-up were acquired from eight patients. Treatment approaches were individually adapted according to good clinical practice and patients' needs. For thin or slightly hyperkeratotic AK either of two modalities was employed: ingenol mebutate 0.015% gel (Picato[®], Leo) once daily for 3 consecutive days to treat 25 cm² skin areas with AK or a modified daylight PDT method for “field” treatment (2 h closed application of methyl aminolevulinate 16% cream [Metvix[®], Galderma] followed by 30 min exposure to daylight) [39,40]. Cryosurgery (open spray, liquid N₂, two cycles of 10 s each) was applied in solitary, hyperkeratotic AK, or in combination with topical application of imiquimod 5% cream (immunocryosurgery) when field treatment was indicated [41].

During image acquisition attention was given to capture almost the same field before and after treatment. For AK quantification, an internal point was selected manually as a reference point in the baseline image, and the examined region was evaluated by the discrimination model. The polar coordinates of the upper left corner of the region to the reference point were estimated (Fig. 5, top). In the follow-up image, the same internal point was manually selected, and the corresponding region was auto-selected based on the same polar coordinates used in the previous baseline image for the upper left corner of the region box (Fig. 5, bottom).

3. Results

3.1. ROI-level evaluation of the SVM_{LBP} model

Table 2 summarizes the performance of the SVM_{LBP} model in three color spaces, namely RGB, YIQ and CIE-Lab. Employing the leave-one-patient-out method, YIQ and CIE-Lab color spaces exhibited similar discrimination accuracy, and generally both outperformed RGB. To select the most informative color components of a color space, we tested all possible color combinations within each space in one, two and three-dimensional configurations. Results for YIQ and CIE-Lab spaces are given in Table 2.2 and 2.3. The combination of Y and I components from the YIQ color space yielded the highest discrimination rates with sensitivity and specificity of 80.2% and 80.1%, respectively (Table 2.2).

The best configuration of the color texture operator $LBP_{P,R}^{riu2}$ was achieved with circular neighborhood $P = 8$ and radius $R = 1$.

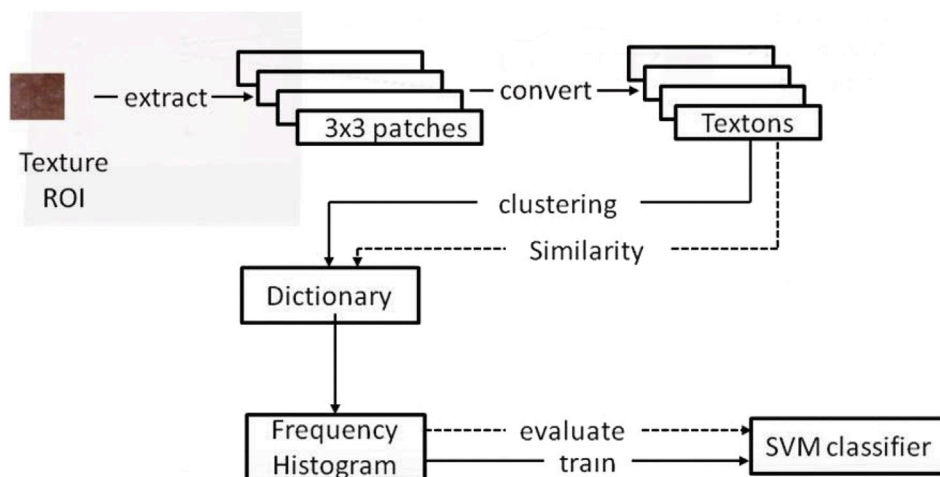


Fig. 4. Overview of texton-based feature extraction and classification. Dashed paths signify the classifier evaluation procedure.

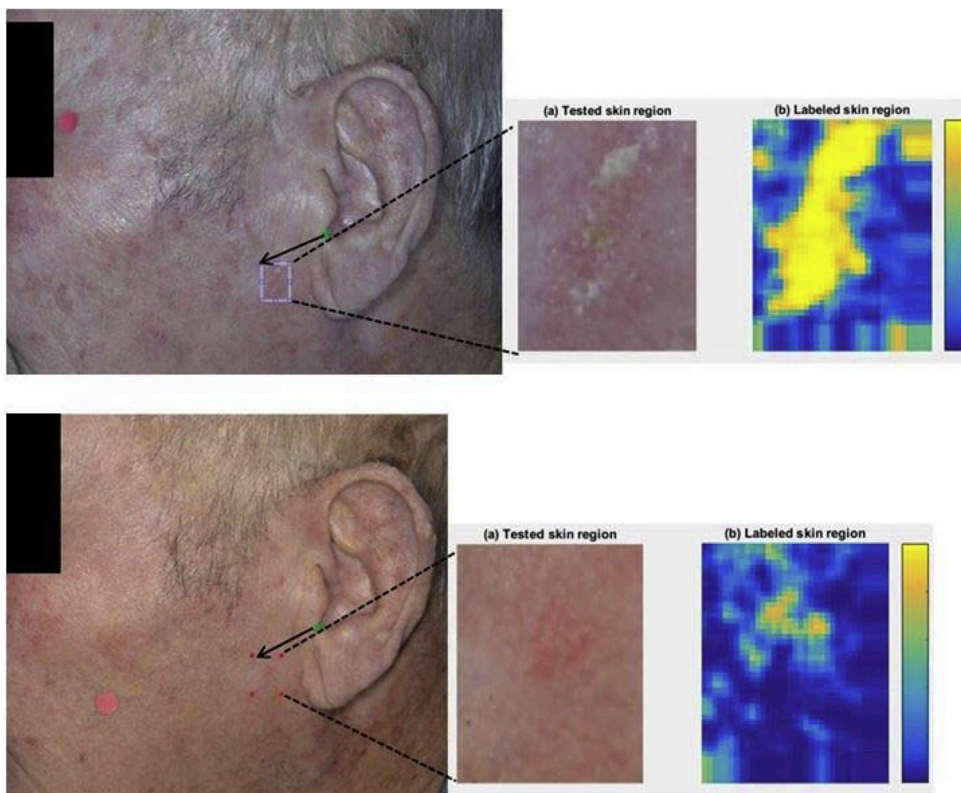


Fig. 5. Application of the model to quantify treatment effects (example from patient 1, Table 4). **Top:** Finding at baseline. (a) A tested region box of 450×350 pixels was selected and the polar coordinates of the upper left corner were estimated using an internal reference point (green point). (b) The selected region was separated into 1271 50×50 pixel windows (10 pixel overlap) and was model-evaluated and quantified; 43.2% (549/1271) of the windows are positive. **Bottom:** The same area at a follow-up appointment 4 months post-treatment. (a) The tested region box was re-identified and auto-selected (red points) using the polar coordinates of the upper left corner to the reference point (green point). (b) The region was model-evaluated and quantified; only 9.8% of the windows (25/1271) were now positive, corresponding to a 77.3% improvement in AK burden. (For interpretation of the references to colour in this figure legend, the reader is referred to the web version of this article.)

Finally, the SVM_{LBP} classification model was implemented using an RBF kernel parameter γ equal to 10 and box constraint parameter C equal to 1.

Since the number of healthy skin patterns was selected equal to that of AK patterns, the prior probabilities and classification costs were set equal for both classes.

3.2. ROI-level evaluation of the $SVM_{Textons}$ model

To construct the codebook of textons, small local patches of 3×3 pixels were randomly extracted from each ROI in the training set. Each 3×3 color patch forms a vector in a $d \times 9$ dimensional feature space where d is the number of color channels used from the YIQ color model. These patch vectors were clustered using the k-means algorithm with $k = 35$ codewords.

Comparative recognition results of AK lesions using texton descriptors are given in Table 2.4. The best accuracy levels were achieved using all components of the YIQ color space, reaching 79.6% and 73.8% for AK and healthy skin, correspondingly.

3.3. Region-level evaluation of the SVM_{LBP} model

The $SVM_{LBP^{mu2}_{8,1}}$ discrimination model, using as inputs concatenated individual Y and I color channel LBP histograms from 50×50 sliding windows, was tested for correctly recognizing skin regions from each patient; 141 out of 157 AK regions (89.8%) and 198 out of 216 healthy skin regions (91.7%) were correctly recognized. Results are summarized in Table 3. Representative examples of misrecognized skin regions are depicted in Fig. 6.

3.4. Evaluation of AK treatment outcome: a preliminary study

Photographs at baseline and during follow-up were acquired from eight patients who were not included in the training set of the model (Table 4).

In six out of the eight patients, multiple lesion fields were evaluated resulting in a total of 32 skin areas selected for the evaluation of treatment outcomes. Fig. 5 depicts the evaluation outcome of selected skin regions, before and after treatment (patient 1: multiple lesions; patient 2: a single lesion). Based on the classifier results, individualized, best practice, minimally invasive interventions yielded an average AK burden reduction of 83.6% (Table 4).

4. Discussion

Clinical photography is widely available and is currently considered essential for the documentation of dermatologic conditions. In conjunction with computer vision techniques it could be upgraded to a fundamental and cost-effective tool for the evaluation of various skin lesions, monitoring disease progression as well as quantifying treatment interventions [22,23,42–47].

In the present study, we explored the utility of clinical photographs in the assessment of AK, a frequent cutaneous premalignancy. We employed an SVM classifier and color texture features to discriminate between AK lesions and healthy skin and to quantify field-directed treatment interventions.

In a different, computer-aided diagnosis approach, Boone et al. [16] have quantified OCT images of facial AK/sSCC lesions. Applying receiver operating curves to determine the cut-off values of the optical characteristics of lesions, they proposed a decision tree diagnostic algorithm for

Table 2

SVM_{LBP} and SVM_{Textons} model performance in color spaces. 2.1 Classification rates using color operator $LBP_{8,1}^{riu2}$ in different color spaces. 2.2 Classification results using color operator $LBP_{8,1}^{riu2}$ and color channel combinations in the YIQ color space. 2.3 Classification results using color operator $LBP_{8,1}^{riu2}$ and color channel combinations in CIE-Lab color. 2.4 Classification results using color texton operator and color channel combinations in the CIE-Lab color space. The approach with the best discriminating performance is depicted in bold.

	Sensitivity (%)	Specificity (%)
2.1	$LBP_{8,1}^{riu2}$	
RGB	75.5	78.3
YIQ	79	82.3
CIE-Lab	78	82
2.2	$LBP_{8,1}^{riu2}$	
YIQ-Y	79	75.8
YIQ-I	73	66.7
YIQ-Q	68.5	68.40
YIQ-IQ	71.7	75.3
YIQ-YI	80.2	80.1
YIQ-YQ	75.8	79
2.3	$LBP_{8,1}^{riu2}$	
LAB-L	79.3	76.1
LAB-A	76.3	73.20
LAB-B	73.2	65.6
LAB-AB	78	79
LAB-LA	78.3	80.3
LAB-LB	77.3	78.7
2.4	Textons	
YIQ-Y	68.6	79.2
YIQ-I	63.7	72.1
YIQ-Q	73.3	67.2
YIQ-IQ	73	71.4
YIQ-YI	69.7	76.9
YIQ-YQ	70.5	73.3
YIQ-YIQ	79.6	73.8

the discrimination of sun-damaged facial skin from AK subtypes and sSCC. The diagnostic accuracy was high (>90%), yet these optimum outcomes were acquired only in the training set. Horn et al. [17] have studied RCM criteria for the discrimination of AK from normal skin. Two observers visually assessed the presence or absence of selected RCM features and classification trees were used to differentiate AK from normal skin. Thus with a single RCM feature (“irregular keratinocyte cell borders”) sensitivity and specificity of 86.67% and 85%, respectively, in the discrimination of AK from healthy skin were achieved. With the integration of additional features into the model, specificity increased up to 90%. However, when considered separately, none of the evaluated RCM criteria were more than moderately reliable for the recognition of AK (interobserver agreement; kappa statistic). Huerta-Brogeras et al. [18] have proposed a diagnostic algorithm that combines the dermoscopic signs “follicular openings” and “erythematous pseudo network” for the diagnosis of AK with 95.6% sensitivity and 95% specificity compared to histopathology. However, evaluation of dermoscopic images was subjective, based exclusively on clinical assessments by experts, and interobserver variability was not reported. McDonagh et al. [19] have used a dimensional imaging dense stereo capture system to obtain 3D shape features to distinguish between neoplastic non-melanoma skin lesions automatically. Feeding depth and color image features into a Bayesian classifier, they demonstrated improved classification rates for five common classes of skin lesions: AK, sSCC, BCC, seborrheic keratosis and melanocytic nevus. They reported an overall method accuracy of 83%. Regarding the AK class, the recognition rate was 100% with, however, the restriction that only 11 samples were analyzed.

The application of standard clinical photography in the evaluation of keratinocytic premalignancies has been previously investigated by Ballerini et al. [22]. A K-NN hierarchical scheme, using color and texture information from clinical photographs, attained an overall classification

accuracy of 74% over the five most common benign and malignant skin growths (malignant melanoma, AK, BCC, melanocytic nevus/mole, sSCC and seborrheic keratosis). Regarding AK, most test images were misclassified as BCC. In a more recent study, Hames et al. [23] proposed a method for automatic AK border delineation on clinical photographs using color space transformations and morphological operations. Automatic segmentation was compared with expert annotation of the pictures, also taking into account intraobserver variability. Correlation between automatic and manual AK identification was 0.62 for face and 0.51 for arm lesions. The sensitivity of automatic detection was 39.5% and 53.1% and the positive predictive values 13.9% and 39.8% for facial and arm AK, respectively.

AK arise multifocally in the initiated epidermis of photo-damaged skin as small clusters of mutated cells [48] that may expand horizontally and vertically within the epidermis for various periods until they become clinically evident [49]. Consequently, the affected skin harbors multiple subclinical disease foci, in addition to clinically recognizable AK [50]. Thus, in most cases, the presence of overt AK in a skin area indicates the presence of an underlying skin cancerization field [51]. “Field therapies” such as PDT and topical ingenol mebutate are principally designed to target exactly these skin areas as a whole, addressing obvious as well as subclinical premalignant lesions [52]. For these reasons, in the present work, we did not attempt to strictly define the borders of individual, clinically demarcated AK lesions but rather addressed the discrimination of AK-affected areas from healthy skin and quantification of the cumulative AK burden within selected skin areas.

The proposed SVM classification model employing LBP color texture features exhibited sensitivity and specificity over 80% at both ROI- and region-based levels (Tables 2.2 and 3) and was also validated in eight patients not included in the training set (Table 4, Fig. 7). In this latter group the model adequately enabled the quantification of treatment efficacy and recorded an averaged 83.6% AK reduction.

Commenting misclassification, the primary source of false negatives were lesions with subtle texture sub-areas interposed by smoothed areas with erythema (Fig. 6, top). However, this “pattern” of lesions appeared only in one patient (out of 22), and possibly our model was insufficiently trained to recognize these lesions. Following, the majority of false positives (Fig. 6, bottom) was mainly recorded from patients with severe photodamage and field carcinogenesis with multiple concurrent keratinocytic carcinomas. Though, this clinical background also challenges the capability of experts to delineate lesions from healthy areas.

Herein, color LBP descriptors have been employed for the identification of morphological alterations of AK lesions. $LBP_{8,1}^{riu2}$ color texture features extracted from the Y and I components of the YIQ color space resulted in the best feature vector to use in the discrimination model. Color LBP and texton descriptors outperformed the conventional grayscale texture analysis (Tables 2.2 and 2.4). Notably, the luminance component Y of the YIQ color space represents grayscale information.

Our results are in line with the current findings indicating that color information plays an important role in texture analysis and can be used to improve recognition performance considerably [29,53]. Compared to textons, the LBP approach exhibited better identification performance in addition to shorter computation times. A possible drawback of this approach is that patch exemplars are not rotationally invariant. However, it has been demonstrated that incorporating rotation-invariant textons, improves, even slightly, their classification performance [31]. Furthermore, LBP descriptors have distinctive robustness against monotonic

Table 3

Confusion matrix for AK versus healthy skin regions; 141/157 AK regions (89.8%) and 198/216 healthy regions (91.7%) were correctly recognized.

Clinically diagnosed regions	Model-recognized regions		Total
	AK	Healthy skin	
AK	141 (89.8%)	16	157
Healthy skin	18	198 (91.7%)	216

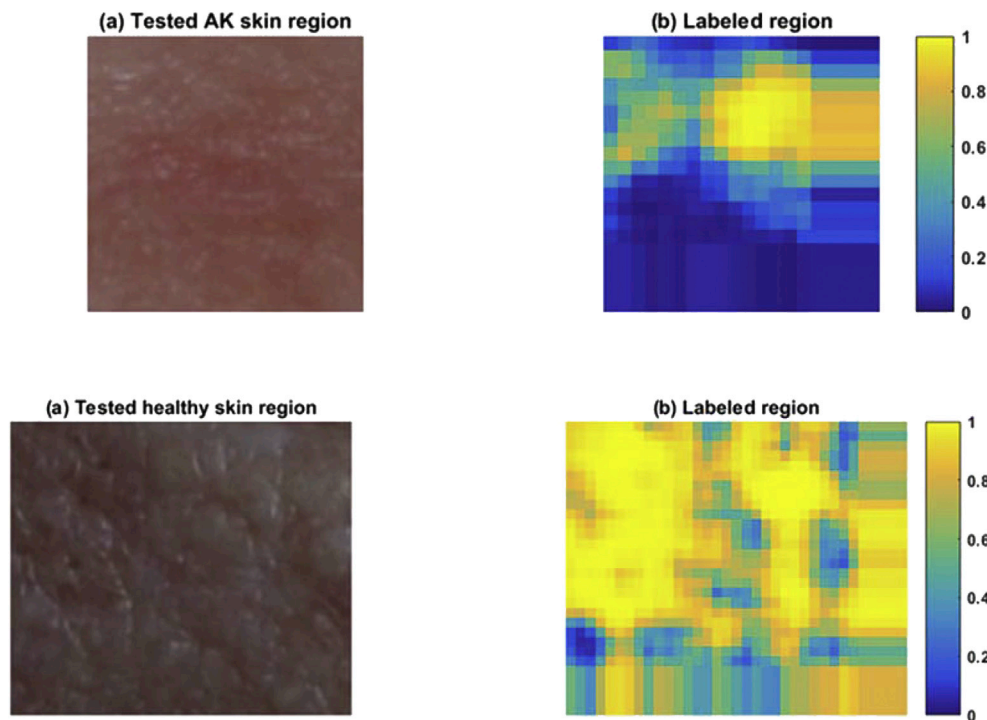


Fig. 6. Examples of misrecognized skin regions. **Top:** (a) A tested AK skin region of 220×222 pixels was separated into $256 \ 50 \times 50$ pixel windows (10 pixel overlap). (b) The majority of the windows were negatively misclassified (161/256; 62.9%), and the whole skin region was misrecognized as healthy skin (False negative). **Bottom:** (a) A tested healthy skin region of 316×368 pixels was separated into $806 \ 50 \times 50$ pixel windows (10 pixel overlap). (b) The majority of the windows were positively misclassified (687/806; 85.2%), and the whole region was misrecognized as AK lesion (False positive).

Table 4
Quantitative evaluation of AK lesions before and after treatment using the SVM_{LBP} discrimination model.

Patient	Sex	Age	Treatment	AK localization	Follow-up (months)	AK burden in % ^a			
						Before treatment	After treatment	AK reduction	Mean AK reduction
1	M	85	Daylight PDT ^b , imiquimod, cryosurgery	Left mandible-preauricular area	4	43.2	9.8	77.3	71.8
						57.2	16.9	70.5	
						24.2	7.8	67.8	
				Forehead (left half)	4	72.9	37.1	49.1	74.6
						43.3	0	100.0	
						43.4	0	100.0	
Forehead (right half)	7	66.7	5.5	91.8	95.9				
		95.7	21.5	77.5					
		96	28	70.8					
2	M	75	Cryosurgery	Right cheek	10	71	6.5	90.8	77.5
						93	14	84.9	
						64	32	50.0	
						63	1	98.4	
						61	0	100.0	
						100	2	98.0	
3	M	79	Ingenol mebutate	Left cheek	2	96	28	70.8	82.2
						71	6.5	90.8	
						93	14	84.9	
				Right cheek	2	64	32	50.0	74.2
						63	1	98.4	
						61	0	100.0	
Forehead	2	100	2	98.0	99.0				
		45.2	5.5	87.8					
		49.4	23.2	53.0					
4	M	82	Imiquimod, cryosurgery	Right cheek	4	56	2.7	95.2	87.8
						40.6	13.5	66.7	
						66.6	1.5	97.7	
						72.2	0	100.0	
						98	20	79.6	
						95.5	44	53.9	
5	M	79	Ingenol mebutate	Occipital	12	92	11.7	87.3	82.5
						18.7	2	89.3	
						29.6	2.8	90.5	
						62.5	10.7	82.9	
						68.3	0	100.0	
						64.5	0	100.0	
6	M	78	Ingenol mebutate	Right cheek	2	66.7	7.1	89.4	73.6
						66	11.6	82.4	
						63.4	6.7	89.4	
						64.1	10.8	83.5	
						64.1	10.8	83.5	
						64.1	10.8	83.5	
7	M	89	Cryosurgery, ingenol mebutate	Forehead (left half)	2	66.7	7.1	89.4	92.5
						66	11.6	82.4	
						63.4	6.7	89.4	
						64.1	10.8	83.5	
						64.1	10.8	83.5	
						64.1	10.8	83.5	
8	M	84	Cryosurgery, ingenol mebutate	Temporoparietal region (left)	2	66.7	7.1	89.4	89.4
						66	11.6	82.4	
						63.4	6.7	89.4	
				Occipital	2	64.1	10.8	83.5	85.9
						64.1	10.8	83.5	
						64.1	10.8	83.5	
Mean						64.1	10.8	83.5	83.6

^a % skin area recognized as AK.

^b Photodynamic therapy.

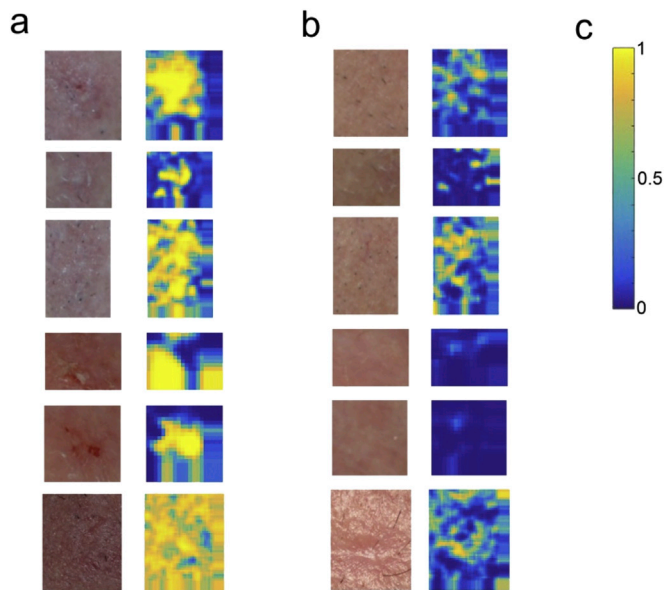


Fig. 7. Monitoring skin regions before (a) and after treatment (b). The first five examples from the top were from patient 1 and the last ones from patient 2 (Table 4). In each pair of figures, the left one is the selected region of the clinical photograph and the right one depicts the AK burden in this field. (c) Employed color bar: a pseudocolor was assigned using a color map that corresponds the probability value of 0 (healthy class) to blue and the probability value of 1 to yellow (AK class). (For interpretation of the references to colour in this figure legend, the reader is referred to the web version of this article.)

illumination changes and this applies in clinical practice where images are captured under varying illumination conditions. However, by assuming that the illumination in a small ROI of 50×50 pixels is approximately uniform (monotonic), we can suggest that LBP descriptors could accommodate potential local intensity fluctuations.

Regarding time efficiency, the computation time of an LBP histogram in a 50×50 pixel ROI was 0.02 s, whereas the corresponding time of an equivalent texton histogram was 0.08 s. To give a concrete example comparing the time efficiency of LBP- and texton-based feature extraction we assumed the assessment of a skin region of 250×200 pixels which is a skin area of 50×40 mm² (e.g. Fig. 3, top). This region was separated into 336×50 pixel windows. Consequently, the estimation time of the AK burden for this example was about 6 s using LBP and about 36 s using the texton approach.

In conclusion, clinical photography combined with relevant image analysis algorithms is a promising non-invasive, cost-effective monitoring tool for the evaluation of field-directed treatment interventions for AK. Moreover, the discrimination power and the fast computation of color LBP features render the herein proposed SVM_{LBP} model a viable and real-time method for evaluating treatment outcomes.

Appendix A. Supplementary data

Supplementary data related to this article can be found at <http://dx.doi.org/10.1016/j.compbmed.2017.07.001>.

References

- [1] L.H. Goldberg, A.J. Mamelak, Review of actinic keratosis. Part I: etiology, epidemiology and clinical presentation, *J. Drugs Dermatol.* 9 (2010) 1125–1132.
- [2] S.J. Salasche, Epidemiology of actinic keratoses and squamous cell carcinoma, *J. Am. Acad. Dermatol.* 42 (2000) 4–7.
- [3] J. Malvehy, A new vision of actinic keratosis beyond visible clinical lesions, *J. Eur. Acad. Dermatol. Venereol.* 29 (2015) 3–8, <http://dx.doi.org/10.1111/jdv.12833>.
- [4] V.D. Criscione, M.A. Weinstock, M.F. Naylor, C. Luque, M.J. Eide, S.F. Bingham, Department of veteran affairs topical tretinoin chemoprevention trial group, actinic keratoses: natural history and risk of malignant transformation in the veterans affairs topical tretinoin chemoprevention trial, *Cancer* 115 (2009) 2523–2530, <http://dx.doi.org/10.1002/cncr.24284>.
- [5] P.J.F. Quaedvlieg, E. Tirsi, M.R.T.M. Thissen, G.A. Krekels, Actinic keratosis: how to differentiate the good from the bad ones? *Eur. J. Dermatol.* 16 (2006) 335–339.
- [6] D.S. Rigel, L.F. Stein Gold, The importance of early diagnosis and treatment of actinic keratosis, *J. Am. Acad. Dermatol.* 68 (2013) S20–S27, <http://dx.doi.org/10.1016/j.jaad.2012.10.001>.
- [7] R. Marks, The role of treatment of actinic keratoses in the prevention of morbidity and mortality due to squamous cell carcinoma, *Arch. Dermatol.* 127 (1991) 1031–1033.
- [8] R.M. Hurwitz, L.E. Monger, Solar keratosis: an evolving squamous cell carcinoma. Benign or malignant? *Dermatol. Surg.* 21 (1995) 184, <http://dx.doi.org/10.1111/j.1524-4725.1995.tb00141.x>.
- [9] K.C. Lee, R. Lew, M.A. Weinstock, Improvement in precision of counting actinic keratoses, *Br. J. Dermatol.* 170 (2014) 188–191, <http://dx.doi.org/10.1111/bjd.12629>.
- [10] S.C. Chen, N.D. Hill, E. Veledar, S.M. Swetter, M.A. Weinstock, Reliability of quantification measures of actinic keratosis, *Br. J. Dermatol.* 169 (2013) 1219–1222, <http://dx.doi.org/10.1111/bjd.12591>.
- [11] M. Ianhez, L.F.F. Fleury Junior, E. Bagatin, H.A. Miot, The reliability of counting actinic keratosis, *Arch. Dermatol. Res.* 305 (2013) 841–844, <http://dx.doi.org/10.1007/s00403-013-1413-y>.
- [12] M. Emre Celebi, W.V. Stoecker, R.H. Moss, Advances in skin cancer image analysis, *Comput. Med. Imaging Graph* 35 (2011) 83–84, <http://dx.doi.org/10.1016/j.compmimag.2010.11.005>.
- [13] I. Maglogiannis, C.N. Doukas, Overview of advanced computer vision systems for skin lesions characterization, *IEEE Trans. Inf. Technol. Biomed.* 13 (2009) 721–733, <http://dx.doi.org/10.1109/TITB.2009.2017529>.
- [14] K. Korotkov, R. Garcia, Computerized analysis of pigmented skin lesions: a review, *Artif. Intell. Med.* 56 (2012) 69–90, <http://dx.doi.org/10.1016/j.artmed.2012.08.002>.
- [15] T.M. Jorgensen, A. Tycho, M. Mogensen, P. Bjerring, G.B.E. Jemec, Machine-learning classification of non-melanoma skin cancers from image features obtained by optical coherence tomography, *Ski. Res. Technol.* 14 (2008) 364–369, <http://dx.doi.org/10.1111/j.1600-0846.2008.00304.x>.
- [16] M.A.L.M. Boone, M. Suppa, A. Marneffe, M. Miyamoto, G.B.E. Jemec, V. Del Marmol, A new algorithm for the discrimination of actinic keratosis from normal skin and squamous cell carcinoma based on *in vivo* analysis of optical properties by high-definition optical coherence tomography, *J. Eur. Acad. Dermatol. Venereol.* 30 (2016) 1714–1725, <http://dx.doi.org/10.1111/jdv.13720>.
- [17] M. Horn, A. Gerger, V. Ahlgrimm-Siess, W. Weger, S. Koller, H. Kerl, H. Samonigg, J. Smolle, R. Hofmann-Wellenhof, Discrimination of actinic keratoses from normal skin with reflectance mode confocal microscopy, *Dermatol. Surg.* 34 (2008) 620–625, <http://dx.doi.org/10.1111/j.1524-4725.2008.34195.x>.
- [18] M. Huerta-Brogeras, O. Olmos, J. Borbujo, A. Hernández-Núñez, E. Castaño, A. Romero-Maté, D. Martínez-Sánchez, C. Martínez-Morán, Validation of dermoscopy as a real-time noninvasive diagnostic imaging technique for actinic keratosis, *Arch. Dermatol.* 148 (2012) 1159, <http://dx.doi.org/10.1001/archdermatol.2012.1060>.
- [19] S. McDonagh, R. Fisher, J. Rees, Using 3D information for classification of non-melanoma skin lesions, in: *Proc. Med. Image Underst. Anal, BMVA Press, 2008*, pp. 164–168. BT-Proc. Medical Image Understanding and.
- [20] B. Jung, Dermatological feasibility of multimodal facial color imaging modality for cross-evaluation of facial actinic keratosis, *Ski. Res. Technol.* (2011) 4–10, <http://dx.doi.org/10.1111/j.1600-0846.2010.00464.x>.
- [21] C. Wassef, B.K. Rao, Uses of non-invasive imaging in the diagnosis of skin cancer: an overview of the currently available modalities, *Int. J. Dermatol.* 52 (2013) 1481–1489, <http://dx.doi.org/10.1111/ijd.12159>.
- [22] L. Ballerini, R. Fisher, B. Aldridge, J. Rees, A color and texture based hierarchical K-NN approach to the classification of non-melanoma skin lesions, *Color Med. Image Anal.* (2013) 63–86, http://dx.doi.org/10.1007/978-94-007-5389-1_4.
- [23] S.C. Hames, S. Sinnya, J.M. Tan, C. Morze, A. Sahebhan, H.P. Soyer, T.W. Prow, Automated detection of actinic keratoses in clinical photographs, *PLoS One* 10 (2015) 1–12, <http://dx.doi.org/10.1371/journal.pone.0112447>.
- [24] H. Byun, S.-W. Lee, Applications of support vector machines for pattern recognition: a survey, *LNCIS* 2388 (2002) 213–236.
- [25] J.M. Moguerza, A. Muñoz, Support vector machines with applications, *Stat. Sci.* 21 (2006) 322–336, <http://dx.doi.org/10.1214/088342306000000493>.
- [26] A. Masood, A.A. Al-Jumaily, Computer aided diagnostic support system for skin cancer: a review of techniques and algorithms, *Int. J. Biomed. Imaging* 2013 (2013) 323268, <http://dx.doi.org/10.1155/2013/323268>.
- [27] C. Cortes, V. Vapnik, Support-vector networks, *Mach. Learn* 20 (1995) 273–297, <http://dx.doi.org/10.1007/BF00994018>.
- [28] J.C. Platt, J.C. Platt, Probabilistic outputs for support vector machines and comparisons to regularized likelihood methods, *Adv. Large Margin Classif.* (1999) 61–74.
- [29] A. Drimbarean, P.F. Whelan, Experiments in colour texture analysis, *Pattern Recognit. Lett.* 22 (2001) 1161–1167, [http://dx.doi.org/10.1016/S0167-8655\(01\)00058-7](http://dx.doi.org/10.1016/S0167-8655(01)00058-7).
- [30] T. Ojala, M. Pietikainen, T. Maenpaa, Multiresolution gray-scale and rotation invariant texture classification with local binary patterns, *IEEE Trans. Pattern Anal. Mach. Intell.* 24 (2002) 971–987, <http://dx.doi.org/10.1109/TPAMI.2002.1017623>.
- [31] M. Varma, A. Zisserman, A statistical approach to material classification using image patch exemplars, *IEEE Trans. Pattern Anal. Mach. Intell.* 31 (2009) 2032–2047, <http://dx.doi.org/10.1109/TPAMI.2008.182>.

- [32] P. Kakumanu, S. Makrogiannis, N. Bourbakis, A survey of skin-color modeling and detection methods, *Pattern Recognit.* 40 (2007) 1106–1122, <http://dx.doi.org/10.1016/j.patcog.2006.06.010>.
- [33] J. Yang, C. Liu, L. Zhang, Color space normalization: enhancing the discriminating power of color spaces for face recognition, *Pattern Recognit.* 43 (2010) 1454–1466, <http://dx.doi.org/10.1016/j.patcog.2009.11.014>.
- [34] G. Kaur, K. Joshi, A brief survey about existed segmentation techniques in automatic detection and segmentation of skin melanoma images, *Int. J. Emerg. Res. Manag. Technol.* (2015) 2278–9359.
- [35] O. Lahdenoja, J. Poikonen, M. Laiho, Towards understanding the formation of uniform local binary patterns, *Int. Sch. Res. Not.* 2013 (2013) e429347, <http://dx.doi.org/10.1155/2013/429347>.
- [36] T. Ojala, M. Pietikäinen, T. Mäenpää, Gray scale and rotation invariant texture classification with local binary patterns, In *Pract. 1842, Computer Vision-ECCV (2000)* 404–420, <http://dx.doi.org/10.1007/3-540-45054-8>.
- [37] M. Varma, A. Zisserman, A statistical approach to texture classification from single images, *Int. J. Comput. Vis.* 62 (2005) 61–81, <http://dx.doi.org/10.1007/s11263-005-4635-4>.
- [38] M.J. Gangeh, L. Sørensen, S.B. Shaker, M.S. Kamel, M. de Bruijne, Multiple classifier systems in texton-based approach for the classification of CT images of lung, in: A.C. Bjoern Menze, Georg Langs, Zhown Tu (Eds.), *Med. Comput. Vision. Recognit. Tech. Appl. Med. Imaging Int. MICCAI Work. MCV 2010*, Beijing, China, Sept. 20, 2010, Revis. Sel. Pap, Springer Berlin Heidelberg, 2010, pp. 153–163, http://dx.doi.org/10.1007/978-3-642-18421-5_15.
- [39] S.R. Wiegell, M. Haedersdal, P.A. Philipsen, P. Eriksen, C.D. Enk, H.C. Wulf, Continuous activation of PpIX by daylight is as effective as and less painful than conventional photodynamic therapy for actinic keratoses; a randomized, controlled, single-blinded study, *Br. J. Dermatol.* 158 (2008) 740–746, <http://dx.doi.org/10.1111/j.1365-2133.2008.08450.x>.
- [40] D.M. Rubel, L. Spelman, D.F. Murrell, J.-A. See, D. Hewitt, P. Foley, C. Bosc, D. Kerob, N. Kerrouche, H.C. Wulf, S. Shumack, Daylight photodynamic therapy with methyl aminolevulinic acid cream as a convenient, similarly effective, nearly painless alternative to conventional photodynamic therapy in actinic keratosis treatment: a randomized controlled trial, *Br. J. Dermatol.* 171 (2014) 1164–1171, <http://dx.doi.org/10.1111/bjd.13138>.
- [41] G. Gaitanis, I.D. Bassukas, Immunocryosurgery for nonmelanoma skin cancer: applications and practical tips, in: P. Pasquali (Ed.), *Cryosurgery*, Springer Berlin Heidelberg, Berlin, Heidelberg, 2015, pp. 245–258, http://dx.doi.org/10.1007/978-3-662-43939-5_20.
- [42] P. Spyridonos, G. Gaitanis, M. Tzaphlidou, I.D. Bassukas, Spatial fuzzy c-means algorithm with adaptive fuzzy exponent selection for robust vermilion border detection in healthy and diseased lower lips, *Comput. Methods Programs Biomed.* 114 (2014) 291–301, <http://dx.doi.org/10.1016/j.cmpb.2014.02.017>.
- [43] P. Spyridonos, G. Gaitanis, I.D. Bassukas, M. Tzaphlidou, Evaluation of vermilion border descriptors and relevance vector machines discrimination model for making probabilistic predictions of solar cheilosis on digital lip photographs, *Comput. Biol. Med.* 63 (2015) 11–18, <http://dx.doi.org/10.1016/j.compbiomed.2015.04.024>.
- [44] P. Spyridonos, G. Gaitanis, I.D. Bassukas, M. Tzaphlidou, Gray Hausdorff distance measure for medical image comparison in dermatology: evaluation of treatment effectiveness by image similarity, *Skin. Res. Technol.* 19 (2013) e498–506, <http://dx.doi.org/10.1111/srt.12001>.
- [45] J. Fernández Alcón, C. Ciuhu, W. ten Kate, A. Heinrich, N. Uzunbajakava, G. Krekels, D. Siem, G. de Haan, Automatic imaging system with decision support for inspection of pigmented skin lesions and melanoma diagnosis, *IEEE J. Sel. Top. Signal Process* 3 (2009) 14–25, <http://dx.doi.org/10.1109/JSTSP.2008.2011156>.
- [46] P.G. Cavalcanti, J. Scharcanski, Automated prescreening of pigmented skin lesions using standard cameras, *Comput. Med. Imaging Graph* 35 (2011) 481–491, <http://dx.doi.org/10.1016/j.compmedimag.2011.02.007>.
- [47] W.-Y. Chang, A. Huang, C.-Y. Yang, C.-H. Lee, Y.-C. Chen, T.-Y. Wu, G.-S. Chen, Computer-aided diagnosis of skin lesions using conventional digital photography: a reliability and feasibility study, *PLoS One* 8 (2013) e76212, <http://dx.doi.org/10.1371/journal.pone.0076212>.
- [48] R.J. Berg, H.J. van Kranen, H.G. Rebel, A. de Vries, W.A. van Vloten, C.F. Van Kreijl, J.C. van der Leun, F.R. de Gruijl, Early p53 alterations in mouse skin carcinogenesis by UVB radiation: immunohistochemical detection of mutant p53 protein in clusters of preneoplastic epidermal cells, *Proc. Natl. Acad. Sci. U. S. A.* 93 (1996) 274–278.
- [49] R.M. Szeimies, L. Torezan, A. Niwa, N. Valente, P. Unger, E. Kohl, S. Schreml, P. Babilas, S. Karrer, C. Festa-Neto, Clinical, histopathological and immunohistochemical assessment of human skin field cancerization before and after photodynamic therapy, *Br. J. Dermatol.* 167 (2012) 150–159, <http://dx.doi.org/10.1111/j.1365-2133.2012.10887.x>.
- [50] C.J. Cockerell, Histopathology of incipient intraepidermal squamous cell carcinoma (“actinic keratosis”), *J. Am. Acad. Dermatol.* 42 (2000) 11–17.
- [51] J. Einspahr, D.S. Alberts, M. Aickin, K. Welch, P. Bozzo, T. Grogan, M. Nelson, Expression of p53 protein in actinic keratosis, adjacent, normal-appearing, and non-sun-exposed human skin, *Cancer Epidemiol. Biomarkers Prev.* 6 (1997) 583–587.
- [52] D. de Berker, J.M. McGregor, M.F. Mohd Mustapa, L.S. Exton, B.R. Hughes, British Association of Dermatologists’ guidelines for the care of patients with actinic keratosis 2017, *Br. J. Dermatol.* 176 (2017) 20–43, <http://dx.doi.org/10.1111/bjd.15107>.
- [53] J.Y. Choi, K.N. Plataniotis, Y.M. Ro, Using colour local binary pattern features for face recognition, in: 2010 IEEE Int. Conf. Image Process, IEEE, 2010, pp. 4541–4544, <http://dx.doi.org/10.1109/ICIP.2010.5653653>.